

Simulations of Global Solar Convection with a Fully Compressible CHORUS++ Code

Keiji Hayashi¹

keiji.hayashi@njit.edu

Alexander G. Kosovichev¹

Chunlei Liang²

ABSTRACT

We present initial simulations of the solar convection zone using a fully compressible hydrodynamic CHORUS++ code and discuss preliminary analysis. Fluid dynamics simulation of the global solar convection is a critically important tool to access the dynamics of solar cycle variations. The CHORUS++ code robustly and efficiently solves the fully compressible hydrodynamic equations using a compact local spectral method and semi-unstructured grid system. Using CHORUS++, we simulate, for the first time, the solar convection shell from 0.7 to 0.99 of the solar radius, using the actual values of the total luminosity and the sidereal rotation rate. The simulation results include the longitudinally averaged rotation rate, reasonably agreeing with the observed solar-type differential rotation. The divergence of simulated mass flux infers that the anelastic-type models are appropriate for modeling the global solar convection, except for the outermost part of the Sun, for which the temporal scale of density variation is estimated at an order of days. The spherical harmonics analysis yields that the horizontal flows are dominant in the large-scale structure, and the degree of the anisotropy of the plasma flow is rather small and constant for the small-scale structures and for a wide range of the radius.

Subject headings: The Sun: corona, magnetic fields, solar wind

1. Introduction

Numerical simulations have offered several key assessments to the long-standing question of how plasma flows in the solar convection system influence and contribute to the 11-year solar-cycle variations of the magnetic field.

¹New Jersey Institute of Technology, Newark, NJ, U.S.

²Clarkson University, Potsdam, NY, U.S.

For example, the anelastic hydrodynamics models (e.g., Miesch et al. 2000; Elliott et al. 2000) and those coupling with the magnetic field (e.g., Brun et al. 2004) successfully retrieved several stellar convection structures, such as the solar-like differential rotation (i.e. the faster rotations at low-latitude regions and slower rotations at the high-latitude regions) under some constraints, the meridional circulation (i.e. poleward flows near the surface and counterflows in the deep convection zone) and the laminar flow patterns when the stellar rotation rate is set high. The description of the mean-field MHD approach (e.g., Pipin & Kosovichev 2024) offers a large-scale macroscopic view of azimuthally averaged flows and essential three-dimensional dynamo processes. The influence of the tachocline and the near-surface magnetic field has been studied by means of numerical implicit Large-Eddy Simulations (ILES) (e.g., Guerrero et al. 2016). The observation data analysis quantifies the near-surface plasma motions that manifest various forms of global flows, such as meridional flows and convective flows of different temporal and spatial scales (Rightmire-Upton et al. 2012; Hathaway et al. 2013). A notable novel approach is simulations of hydrodynamics (HD) and magnetohydrodynamics (MHD) with the sound-speed reduction method (e.g., Hotta et al. 2014, 2022), where the mass continuity equation is modified to reduce the sound speed and hence increase the simulation time step. This approach has proved efficient, in particular, in parallel computing because the simulation scheme can be highly localized and compact, while the basic nature of the MHD (or HD) is nearly fully taken into account.

As shown in simulations of the interactions between the magnetic field flux and the plasma in the solar convection zone (e.g. Fan et al. 2003), compressibility may play a key role in the solar convection system. Despite limiting the scope to the HD case, density variations play primary roles in various processes, such as driving and maintaining the turbulent flows in the convection system, particularly in the near-surface rotational shear layer. The material cooled on the solar surface must be heavier because of the local pressure balance, and ultimately, the deviation becomes large enough to break the fragile local hydrostatic balance and start to flow downward. These nonlinear processes are treated correctly when and only when simulated with fully compressible models (e.g., Kitiashvili et al. 2023).

Several factors have prevented the simulations from using the actual solar parameters. When the actual values of the solar luminosity and rotation rate are used, the evolution from the (usually semi-steady) initial state to the global convective flows will be slow. Hence, it is computationally expensive to simulate the solar convection zone with the actual solar parameters. A simulation that includes a near-surface region is challenging because of the very steep gradients of plasma density, temperature, and pressure. So far, it has only been done in local rectangular domains. It requires setting up small grid sizes in the radial direction to treat steep gradients, which requires us to adopt substantially smaller time steps in the ordinary explicit HD or MHD simulation model, leading to more computational costs.

In part to mitigate these computational difficulties, many solar convection models have often used the so-called laminar benchmark case (Jones et al. 2011). A commonly used set of benchmark parameters includes large values of the stellar luminosity and the stellar rotation rate, which en-

hances the growth of convection and hence requires fewer computational resources. The assumption of incompressible flow (i.e., $\nabla \cdot (\varrho \mathbf{V}) = 0$) is often used for the same reasons. Although the simulations with the benchmark setting and/or the incompressible flows (or the reduced-sound-speed methods) successfully find several important aspects of the solar convection zone, it is desired to simulate the solar convection zone with a fully compressible code and with the actual solar parameters. In addition, if we conduct simulations with the compressible simulation, we can assess the appropriateness of the assumption of the divergence-free mass flux currently used in most solar-stellar global HD simulations.

CHORUS++ (Chen et al. 2023) is an improved version of the CHORUS model (Compressible High-Order Unstructured Spectral differencing Wang et al. 2015, 2016). CHORUS has two notable features: the unstructured grid system and the spectral differencing method. CHORUS++ employs a cubed-sphere meshing algorithm (Ronchi et al. 1996) and improves CHORUS from isoparametric mappings to transfinite mappings. As a result, CHORUS++ demonstrated sufficient numerical stability using the 6th- and 7th-order spectral difference methods Chen et al. (2023). The simulated volume is covered by six subdomains without any overlaps or gaps (e.g., Feng et al. 2010); hence, only flux points on a two-dimensional surface are needed to consider for exchanging physical information between the subdomains. The spectral differencing method is a subset of the flux reconstruction/correction procedure (e.g. Kopriva 1994; Sun et al. 2007; Huynh 2007, 2009). Each subdomain is discretized with semi-unstructured spherical grid assignment to avoid severe CFL (Courant–Friedrichs–Lewy) condition. The CHORUS++ code has been demonstrated to have improved computational efficiency over the original CHORUS code on distributed memory CPU systems in (Chen et al. 2023) to solve the benchmark cases of the stellar convection system robustly using a higher order spatial discretization. In this article, we use the CHORUS++ code with a few modifications in the simulation setting: The total stellar luminosity is set to the solar luminosity, the rotation rate is set to the solar mean sidereal rotation, and the inner and outer boundary surfaces are set at $0.70 R_{\odot}$ and $0.99 R_{\odot}$, respectively.

This article is organized as follows. In Section 2, the CHORUS++ code and the simulation setting for this study are given. In Section 3, the simulation results are shown, and several properties of the derived plasma flows in the solar convection zone, such as the flow patterns and the divergence of the mass flux, are examined. In Section 4, the summary and conclusions are given.

2. Simulation Model

CHORUS++ (Chen et al. 2023) uses the explicit five-stage and third-order Runge-Kutta method of stability preservation (SSPRK (5,3)) (Ruuth 2005) to solve the set of equations of a fully compressible fluid in the rotating reference frame at a constant rotation rate ($\boldsymbol{\Omega}_{\odot}$),

$$\frac{\partial \varrho}{\partial t} = -\nabla \cdot (\varrho \mathbf{U}), \tag{1}$$

$$\frac{\partial(\varrho\mathbf{U})}{\partial t} = -\nabla(\varrho\mathbf{U} : \mathbf{U} + P\mathcal{I}) + \nabla(\bar{\tau}) + \varrho\mathbf{g} - 2\varrho\boldsymbol{\Omega}_o \times \mathbf{U}, \quad (2)$$

$$\frac{\partial\mathcal{E}}{\partial t} = -\nabla \cdot (\mathbf{U}(\mathcal{E} + P)) + \nabla(\mathbf{U} \cdot \bar{\tau} - \bar{\mathbf{q}}) + \varrho\mathbf{g} \cdot \mathbf{U}, \quad (3)$$

where ϱ , \mathbf{U} , and \mathcal{E} are the density, velocity vector, and total energy. Under the ideal gas assumption, the gas pressure P is given as $P = \varrho\mathcal{R}T$ with the gas constant \mathcal{R} , and the total energy is given as $\mathcal{E} = \frac{P}{\gamma-1} + \frac{1}{2}\varrho U^2$, with the specific heat ratio $\gamma (= 5/3)$. As in Chen et al. (2023), the centrifugal force is not included in this study.

The shear stress tensor $\bar{\tau}$ is given as

$$\bar{\tau} = \mu(\nabla\mathbf{U} + (\nabla\mathbf{U})^T + \lambda(\nabla \cdot \mathbf{U})\mathcal{I}) \quad (4)$$

with the dynamic viscosity, $\mu = \nu\varrho$ (ν is the kinematic viscosity coefficient), and $\lambda = -(2/3)\mu$. The heat flux \mathbf{b} is given as

$$\mathbf{b} = -\kappa\varrho T\nabla S - \kappa_r\varrho C_p\nabla T \quad (5)$$

with the entropy diffusion coefficient κ and the radiative diffusivity κ_r . The specific entropy S is defined as

$$S = C_p \ln\left(P^{1/\gamma}/\varrho\right) \quad (6)$$

with the specific heat at constant pressure C_p . The extra terms are due to the gravity of the Sun and the Coriolis force.

In the CHORUS++ code, the velocity vector \mathbf{U} is defined in the Cartesian system, $\mathbf{U} = (u, v, w)$ or $\mathbf{U} = (V_x, V_y, V_z)$, and the numerical fluxes normal to the cell faces are calculated through the Bassi-Rebay I scheme Bassi & Rebay (1997). The governing equations in the physical domain are transformed into local coordinates of a computational cell using the transfinite mapping approach. The transfinite mapping approach is a major improvement over the original CHORUS code Wang et al. (2015) because it can represent the curves of the edges and faces of each physical element within the machine precision (Chen et al. 2023). For the initial study, we set the grid size in the radial direction at about $0.003 R_\odot$ and the heliocentric angles of the numerical cells at $0.8 \sim 0.95$ degrees.

2.1. Model parameters, initial values, and simulation setup

We used the same parameters as in the benchmark test case (Chen et al. 2023) except the stellar luminosity, rotation rate, and radius of the upper boundary sphere surface. In conjunction with the change of the radius of the top boundary surface ($r = R_{\text{top}}$), we need to adjust the plasma density there. The parameters set in the presented study are tabulated in Table 1. For reference, the benchmark parameters and some of the actual solar properties are also given in this table.

The initial values are determined in the same manner as described in Chen et al. (2023), where the thermal heat conduction rate (κ_r) is given as a function of the heliocentric distance and the

Table 1: Parameters, constants, and representative numbers for (a) the actual Sun, (b) the presented cases, and (c) the benchmark case. The numbers for the benchmark case are from Chen et al. (2023) (and/or Wang et al. (2015)). The constants are set as follows: Gravitational constant $G = 6.67 \cdot 10^{-8}$ ($\text{cm}^3 \text{g}^{-1} \text{s}^{-2}$), the solar mass $M_\odot = 1.98891 \cdot 10^{33}$ (g), the specific heat ratio $\gamma = 5/3$, the gas constant $\mathcal{R} = 1.4 \cdot 10^8$ ($\text{erg g}^{-1} \text{K}^{-1}$), the specific heat at constant pressure $C_P = 3.5 \cdot 10^8$ ($\text{erg g}^{-1} \text{K}^{-1}$), the solar luminosity $L_\odot = 3.846 \cdot 10^{33}$ (erg s^{-1}), and the solar sidereal rotation rate $\Omega_\odot = 3.0 \cdot 10^{-6}$ (rad s^{-1}). The parameter D is the thickness of the convection zone ($D = R_{\text{top}} - R_{\text{bot}}$).

	(a) the Sun	(b) presented case	(c) benchmark
fixed time step, Δt [s]		2.5	4 ~ 20
Lower bound., R_{bot} in R_\odot	~0.70	0.70	0.70
Upper bound., R_{top} in R_\odot	1	0.99	0.95
Density at $r = R_{\text{bot}}$, ϱ_{top} [$\text{g} \cdot \text{cm}^{-3}$]		$2.1 \cdot 10^{-1}$	$2.1 \cdot 10^{-1}$
Density at $r = R_{\text{top}}$, ϱ_{top} [$\text{g} \cdot \text{cm}^{-3}$]		$2.1 \cdot 10^{-4}$	$1.05 \cdot 10^{-2}$
Den. scale, $N_p = \log_e(\varrho_{\text{bot}}/\varrho_{\text{top}})$	~ 16	6.908 ($\sim \log_e 1000$)	3.0 ($\sim \log_e 20$)
Luminosity L_o	$1 \times L_\odot$	$1.0 \times L_\odot$	$10^3 \times L_\odot$
Rotation rate, Ω_o	$\sim 1 \times \Omega_\odot$	$1.0 \times \Omega_\odot$	$27.0 \times \Omega_\odot$
kinematic viscosity ν [$\text{cm}^2 \text{s}^{-1}$]		$6.0 \cdot 10^{12}$	$6.0 \cdot 10^{13}$
entropy diffusion coef. κ_s [$\text{cm}^2 \text{s}^{-1}$]		$6.0 \cdot 10^{13}$	$6.0 \cdot 10^{13}$
U'_{rms} [$\text{cm} \cdot \text{s}^{-1}$]		$1.51 \cdot 10^4$	$4.04 \cdot 10^4$
ΔS [erg/g/K]		$1.249 \cdot 10^6$	$7.798 \cdot 10^5$
Rayleigh num. $GM_\odot D \Delta S / (\nu \kappa_s C_p)$	10^{20}	$2.670 \cdot 10^7$	$1.429 \cdot 10^6$
Reynolds num. $U'_{\text{rms}} D / \nu$	10^{12}	51.06	11.72
Ekman num. $\nu / (\Omega_0 D^2)$	10^{-14}	$4.853 \cdot 10^{-3}$	$2.447 \cdot 10^{-3}$
Taylor num. $4\Omega_0^2 D^4 / \nu^2$	$10^{19 \sim 27}$	$1.698 \cdot 10^5$	$6.682 \cdot 10^5$
Prandtl num. ν / κ_s	$10^{-6 \sim -4}$	0.1	1
Rossby num. $U'_{\text{rms}} / (2\Omega_0 D)$	$10^{-1 \sim 0}$	$1.239 \cdot 10^{-1}$	$1.433 \cdot 10^{-2}$

density scale (N_p ; the ratio of the mass density at the upper and lower boundary surfaces) must be given. We used the same value of the thermal heat conduction rate and a different value of the density scale (because of the difference in the radius of the top boundary surface, R_{top}).

The initial state is nearly stable except the near-surface regions at $r \sim R_{\text{top}}$ where the plasma structure is unstable to perturbations or fluctuations. Figure 1(e) shows the radial profile of the square of the buoyancy frequency at the initial value,

$$N^2 = g(r) \left[\frac{1}{\gamma} \frac{1}{P_g} \frac{\partial P_g}{\partial r} - \frac{1}{\varrho} \frac{\partial \varrho}{\partial r} \right], \quad (7)$$

where the positive (negative) N^2 indicates that the region is stable (unstable) against perturbations. The initial plasma distribution is unstable at $r > 0.94R_\odot$. The instability gradually grows, and the convective flows ultimately prevail throughout the simulated convection zone.

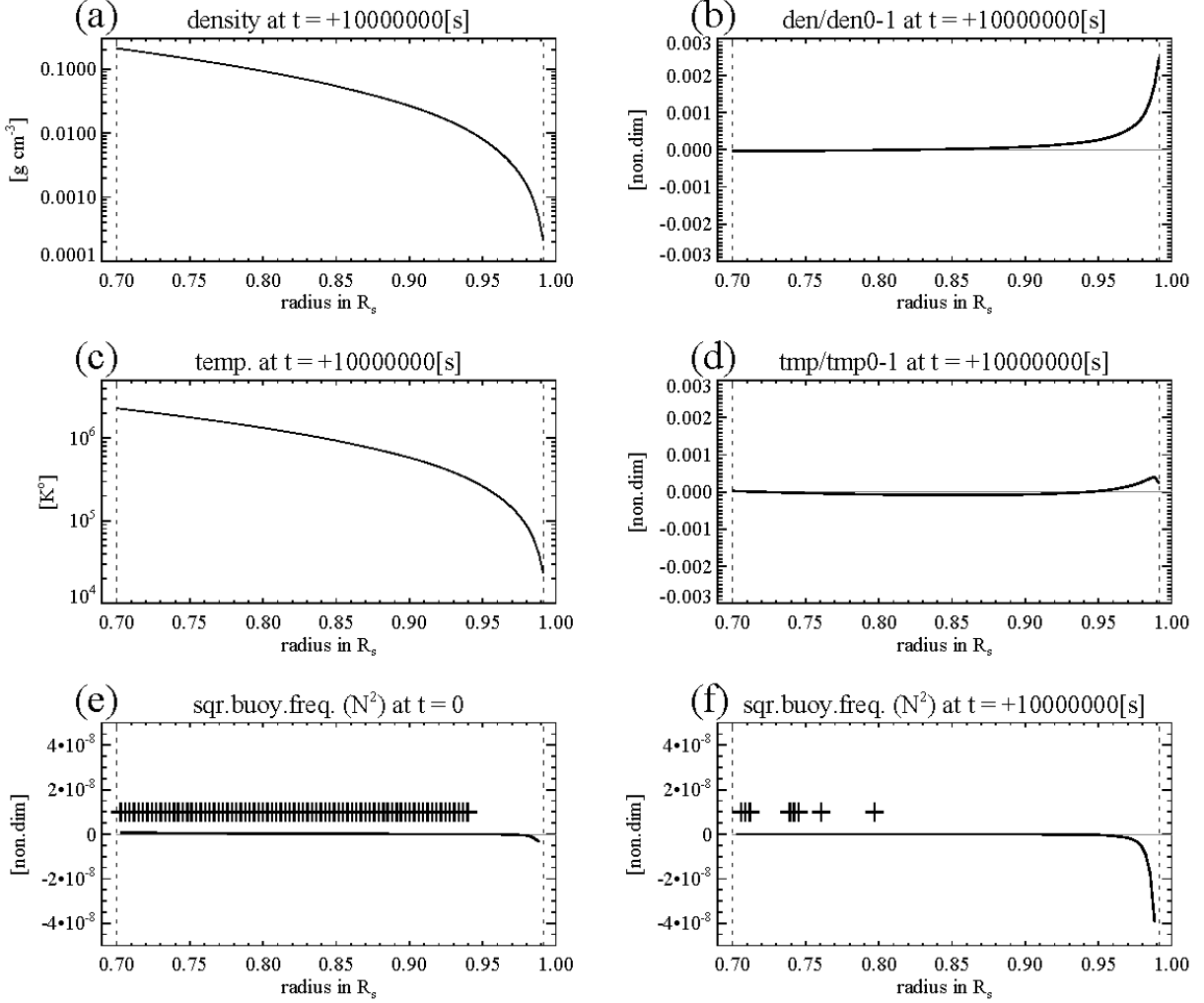


Fig. 1.— Radial profile of the simulated plasma quantities in the solar convective shell: (a) mass density ρ and (c) temperature (T) at $t = 1 \cdot 10^7 s$. In panels (b) and (d), the deviations of the simulated variable from the initial values, ρ_0 and T_0 , are given as $(\rho/\rho_0 - 1)$ and $(T/T_0 - 1)$, respectively. The deviation is less than 10^{-3} overall, except the density deviation reaches about $2 \cdot 10^{-3}$ near the top boundary. In the bottom row, the radial profile of the square of buoyancy frequency (N^2) of the initial value and the buoyancy frequency averaged horizontally (latitudinally and longitudinally) for the state at $t = 10^7 s$ are given in panels (e) and (f), respectively. In these two plots, cross (+) marks are placed where $N^2 > 0$.

Figure 2 demonstrates the radial component of the plasma velocity (V_r) simulated at $t = 1 \cdot 10^7 s$. The convective flows are seen in the simulated convection zone, as well as the convective cell structures on the top boundary surface. In Figure 1(f), the square of the buoyancy frequency N^2 is nearly all negative throughout the simulation volume at the selected moment.

Panels (a) and (c) of Figure 1, respectively, show the radial profile of the mass density and temperature averaged over each shell layer at $t = 1 \cdot 10^7 s$. Panels (b) and (d), respectively, show the ratios of the simulated plasma density and temperature to those of the initial values. Although the simulated system will be in the convective state, the differences in plasma density and temperature are found to be very small. A notable difference is found in the density ratio near the top boundary surface as shown in panel (b); still, the deviation is 0.25% in the largest.

3. Results

The kinetic energy density ($\rho V^2/2$) is a good proxy to represent the entire simulated convective system. In the benchmark case (Chen et al. 2023), the kinetic energy density of the simulated stellar convection zone exhibits exponential growth and a brief overshoot/oversaturation, then reaches a plateau profile that corresponds to the statistically stable saturated convection state.

Figure 3 shows the temporal profile of the kinetic energy density. With the actual solar parameters, the temporal profile of the kinetic energy density is different from that of the benchmark tests. In the logarithmic scale plot, the exponential growth of the energy density is found as a (near) linear line, roughly at $10 \leq t \leq 20$ days. However, the overshooting and the following plateau profile (like those in Figure 7 of Chen et al. 2023) are not clearly seen. The current simulation run has been done only for $t \leq 1.5 \cdot 10^7 s \sim 170$ d, but it is unclear whether or not the kinetic density will become more constant in an extended simulation run. Because our visual inspections did not find distinct differences in the figures for $t = 1 \cdot 10^7 s$ and $t = 1.5 \cdot 10^7 s$, we chose the simulated data at $t = 10^7 s \sim 115$ d as a moderately mature state of the convection properties.

3.1. Large-scale Convection/Granulation Cells

Figure 4(a) shows the deviation of temperature from the averaged value at a selected near-surface depth (at $r = 0.982 R_\odot$ and $t = 1.0 \cdot 10^7 s$).

As shown in Figure 1(b,d), the deviations of the simulated plasma variables from the initial values are relatively small in the radial direction. The temperature, averaged over the selected sphere, was $7.4132 \cdot 10^4 K^\circ$, approximately 8 degrees higher than the initial value, and the largest deviation from the averaged state is about 6.7 degrees. The lower temperature structures are found at the boundaries of the convection cells that can be identified as negative velocity V_r in Figure 4(b). The temperature and plasma motions near the surface are found to be rather uneven

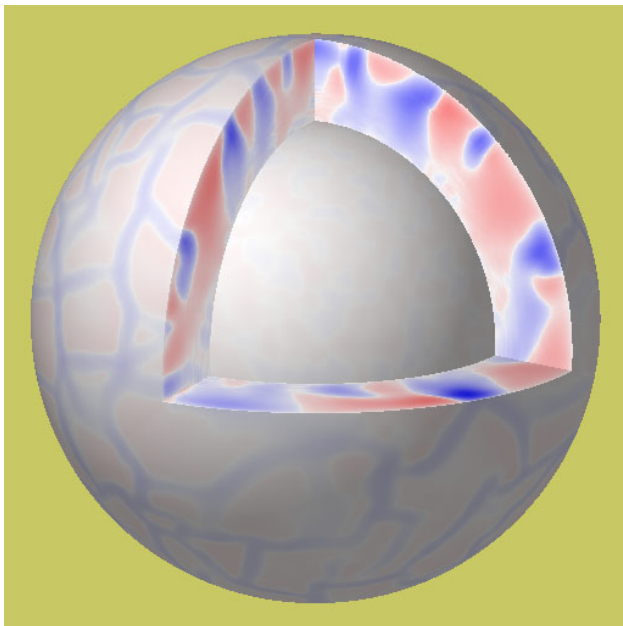


Fig. 2.— The simulated radial component of the plasma flow (V_r) at $t = 10^7$ s. An octant section has been removed to display the meridional and equatorial cross-sections. The red (blue) colors represent the positive (negative) values.

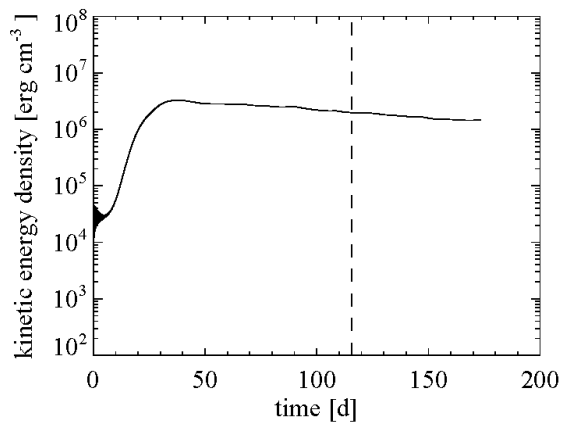


Fig. 3.— Temporal profile of the average kinetic energy density. The vertical dashed line indicates the moment ($t \simeq \cdot 10^7$ s for which most figures in this article are made using the simulation data.

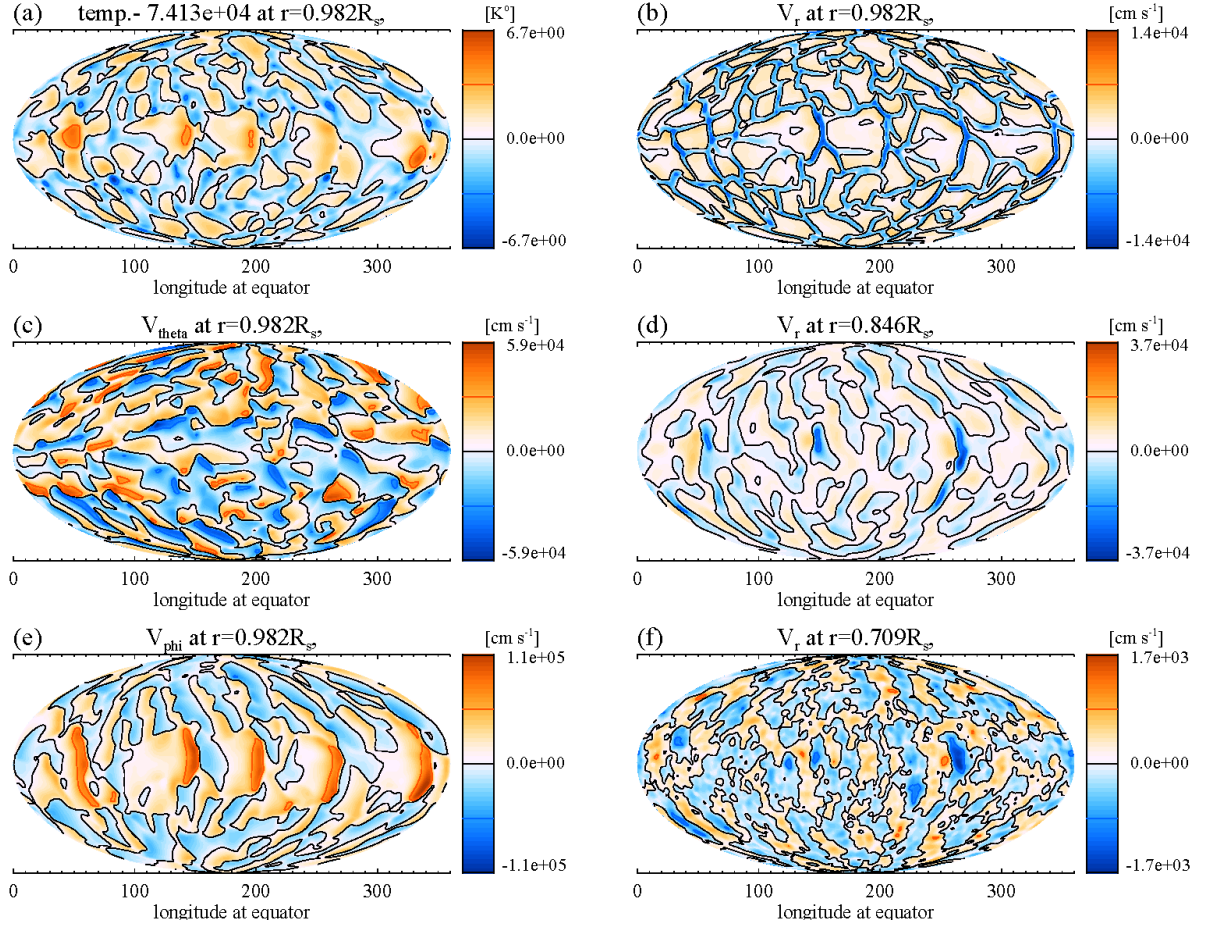


Fig. 4.— The plasma quantities of the simulated solar convection zone at $t = 10^7$ s in the Mollweide projection mapping. (a) The plasma temperature subtracted by the average ($7.4132 \cdot 10^4$ K), (b) the radial component of the plasma flow (V_r), (c) the latitudinal component of the plasma flow (V_{θ}), at $r = 0.982 R_{\odot}$. (e) the longitudinal component of the plasma flow (V_{ϕ}). In the right column, panels (d) and (f) respectively show the radial component of the plasma flows at the middle depth of the simulated convection zone (at $r = 0.846 R_{\odot}$) and near the bottom boundary surface (at $r = 0.709 R_{\odot}$) in the same format as in panel (b). The colors are truncated at the largest absolute value so that the red (for positive values) and blue (for negative values) are assigned evenly across the zero values.

within convection cell structures. For example, the region of relatively high temperature (panel a) and large prograde plasma motion (V_ϕ in panel e) are found in the western (right) part of the convection cells near the equator (panel b). The latitudinal motion (V_θ in panel c) exhibits a weak but similar tendency to V_ϕ ; relatively large poleward flows are found near the boundary of each convective cell close to the poles in each hemisphere. In the right column in Figure 4(b,d,f), the distribution of V_r at different depths is presented. The size and shape of the convection cells differ substantially at different depths, while several strong downward flows are found at the same locations over a wide range of depths.

3.2. Polar regions

Figure 5 offers the north pole view of the simulated plasma flows near the top boundary surface (at $r = 0.982 R_\odot$). Because the CHORUS++ code uses an unstructured grid system, issues due to the geometric singularity like that in the case of the spherical coordinate presentation are not present, and the plasma flows crossing the solar rotation axis (or z -axis) are treated naturally. The snapshot shown (at $t = 1 \cdot 10^7$ s) does not show clear polar vortex cell structures (e.g., discussed by Nagashima et al. 2011; Dikpati et al. 2024). By tuning our future simulation settings, we plan to investigate in more detail the formation of plasma-flow structures in the high-latitude and polar regions that are believed to play a major role in solar-cycle activities.

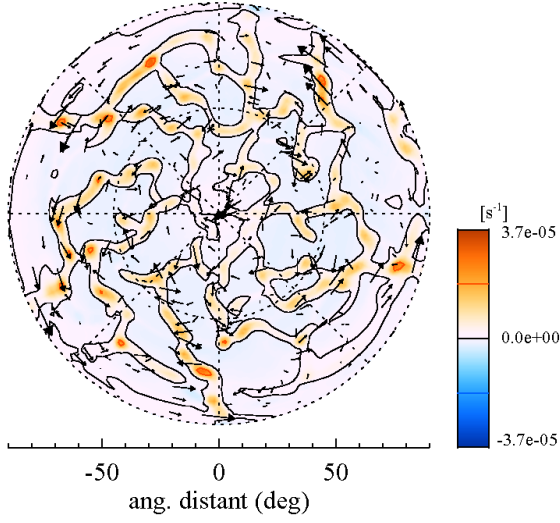
3.3. Meridional Circulation and Rotation

Figure 6 shows the radial and latitudinal components of the plasma flow vector (V_r and V_θ , respectively) and the angular velocity with respect to the simulation coordinate frame, $\omega := V_\phi/r \sin \theta$. In the upper row, the flow components at a selected longitude ($\phi = 180^\circ$) are shown. In panel (a), the downward flows (negative V_r) starting from near the solar surface are overall bent equatorward before reaching deeper layers. A similar trend is found in the longitudinally averaged values shown in panel (d).

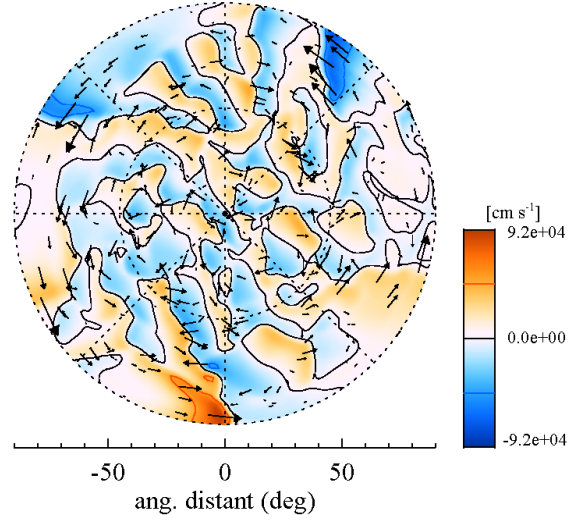
In Figure 6(e), the averaged latitudinal component (V_θ) overall exhibits the equatorward motions near the solar surface. Counter (poleward) flows are found at a relatively shallow depth $r \sim 0.85 R_\odot$ in the northern hemisphere. The values of the latitudinal component V_θ at deeper layers are small. Hence, the patterns of the equatorward bents of V_r seen in panel (a) have been caused by the poleward motion of the near-surface sources rather than the global (averaged) advection motion.

In Figure 6(f), the distributions of the averaged angular rotation rate are more similar to those inferred from observations: faster (prograde) equator rotation near the surface and slower (retrograde) high-latitude motions. The difference between the rotation rates at the solar equator and middle latitude region ($\pm 30^\circ$ from the equator) is about 1.5 degrees per day or 40 degrees per

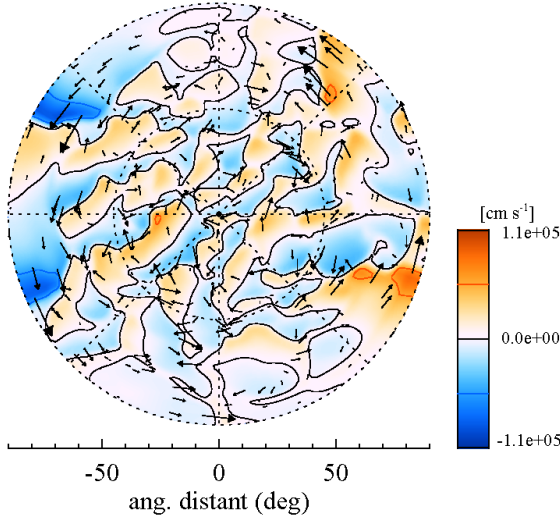
(a) $\text{curl}(\mathbf{V}_h)$ at $r=0.982R_s$



(b) V_x at $r=0.982R_s$



(c) V_y at $r=0.982R_s$



(d) V_z at $r=0.982R_s$

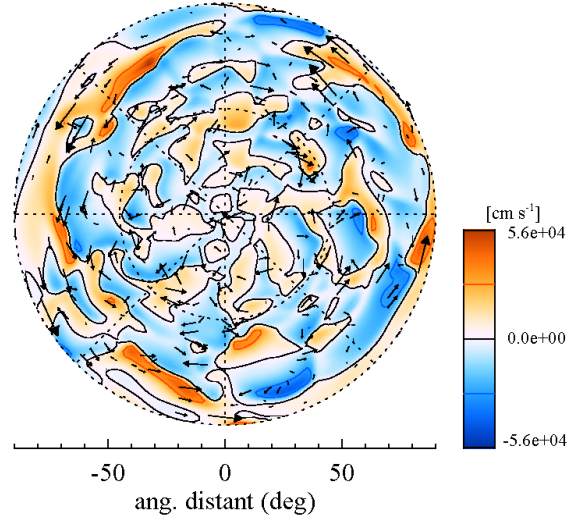


Fig. 5. — (a) the curl of the horizontal flows, (b) — (d) The x , y , and z components of the simulated plasma flows around the north pole.

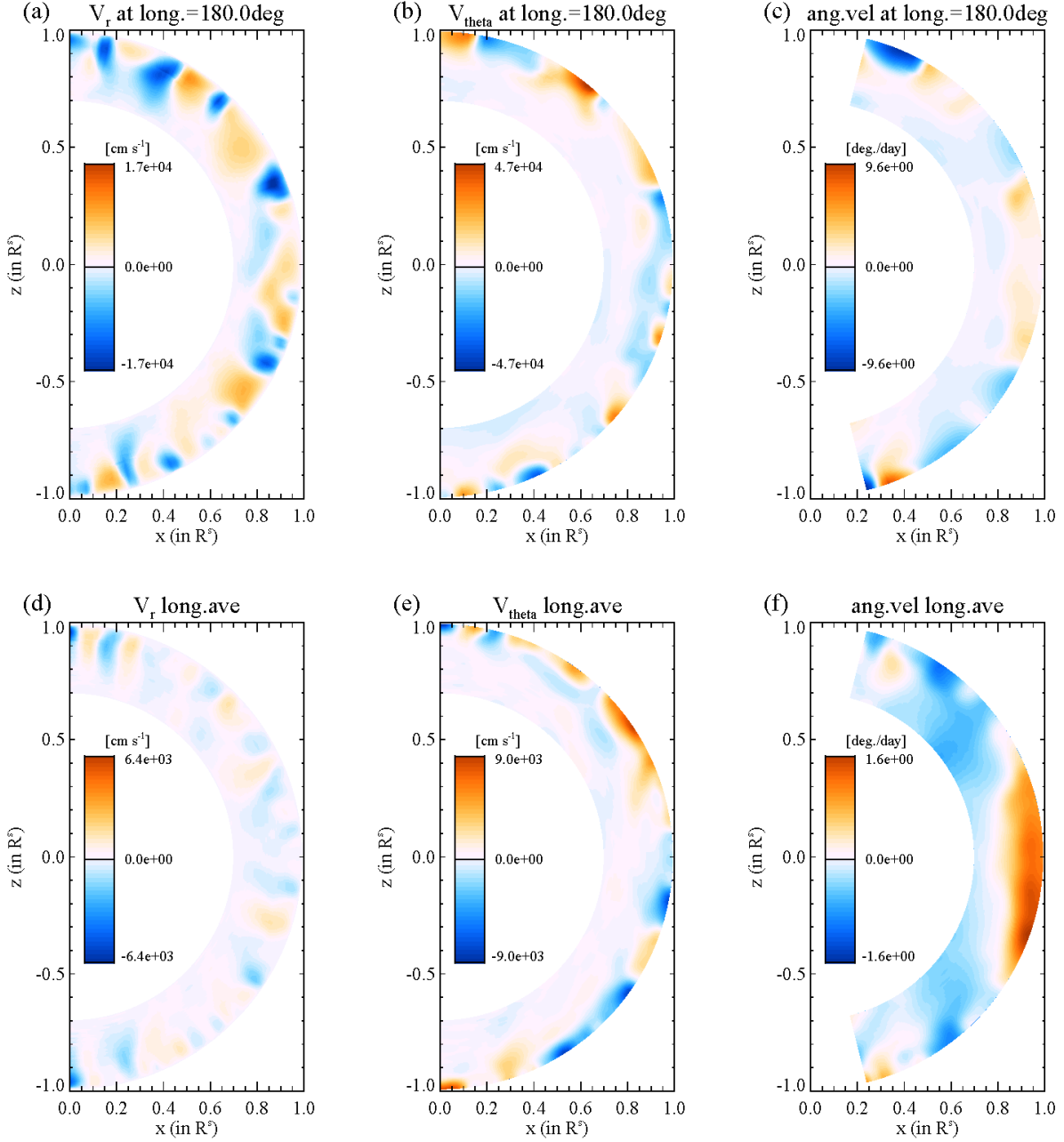


Fig. 6.— Meridional cross-section view of the simulated plasma flows at $t = 10^7 s$. From left, the radial component of the plasma flow (V_r), the latitudinal component (V_θ), and the rotation rate relative to the reference frame ($\omega := V_\phi/(r \sin \theta)$) are shown. In the top row, the plotted values are sampled at a selected longitude ($\phi = 180$ degrees). In the bottom row, the same quantities but averaged over the longitude are shown.

one solar rotation, which is much larger than that of the actual Sun.

3.4. Divergence and vorticity of plasma flows

The present simulation solves the fully compressible HD equations; hence, no assumptions are given to the divergence of the plasma flow, $\nabla \cdot \mathbf{V}$, or the mass flux, $\nabla \cdot (\varrho \mathbf{V})$. Figure 7 shows the latitude-longitude distribution of plasma flows near the top boundary surface. In panels (a) and (b), the divergence of the mass flux and the radial component of the vorticity of the plasma flow vector, $\nabla_h \times \mathbf{V}_h$, are shown, respectively. The convergence (negative divergence) of the mass flux is found at the downward flow (negative V_r) or the boundary of the large-scale granulation cells. In Figure 7(b), the distribution of the radial vorticity exhibits several interesting features. First, the north-south symmetry is noticeable. Second, in the northern hemisphere, the positive $(\nabla \times \mathbf{V})_r$ values are concentrated along the boundaries of the convection cells, while the negative values are found rather evenly within the cells. Because the solar-like differential rotation yields the positive $(\nabla \times \mathbf{V})_r$ in the northern hemisphere, the obtained solar-like differential rotation (shown in panels (c) and (e) of Fig.6) are indeed contributed from the motions of the narrow downward-flow lanes. We think that the concentration of the positive radial vorticity is indeed formed in the divergent flows within each convection cell where the Coriolis force initiates the clockwise motions (viewed from outside) and forms lanes of the large positive vorticity (local counter-clockwise vortices).

Figure 8(a) shows the meridional view of the divergence of the mass flux, $\nabla \cdot (\varrho \mathbf{V})$, averaged in the longitudinal direction. To analyze and quantify the divergence and its spatial distributions, we applied normalization to the divergences. In panel (b), the average of the absolute divergence, $|\nabla \cdot (\varrho \mathbf{V})|$, is shown.

In Figure 8(c), the average of the absolute values is normalized with the average of the mass density, $|\nabla \cdot (\varrho \mathbf{V})| / \langle \varrho \rangle$, so that the normalized value will be in the physical unit of s^{-1} , and the inverse corresponds to the time scale for the divergence of the mass flux to substantially alter the local density. In this case, the larger values are found near the outer boundary surface, meaning that the relative variations of the plasma density are larger in the outer part of the convection zone than near the bottom of the convection zone, which is rather anticipated. The smallest value of the time scale (or the inverse of the largest value of the normalized divergence) is found near the top boundary surface and estimated at about $1.6 \cdot 10^5 s$ or about $1.8 d$. The time scale for the deeper layers is estimated at an order of $10^4 d$. These estimations of time scale imply that the simulations with the divergence-free mass flux can properly handle the simulated system at least for this limit in a spherical convective shell, which does not include near-surface and surface layers. Of course, the size and position of the convective granulation changes quickly, so the practical limit must be much longer.

Figure 8(d) offers the distribution of $|\nabla \cdot (\varrho \mathbf{V})| / \langle \varrho V \rangle$. This quantity has a physical unit of cm^{-1} , and the inverse represents the spatial scale of the contribution of the divergence of the mass

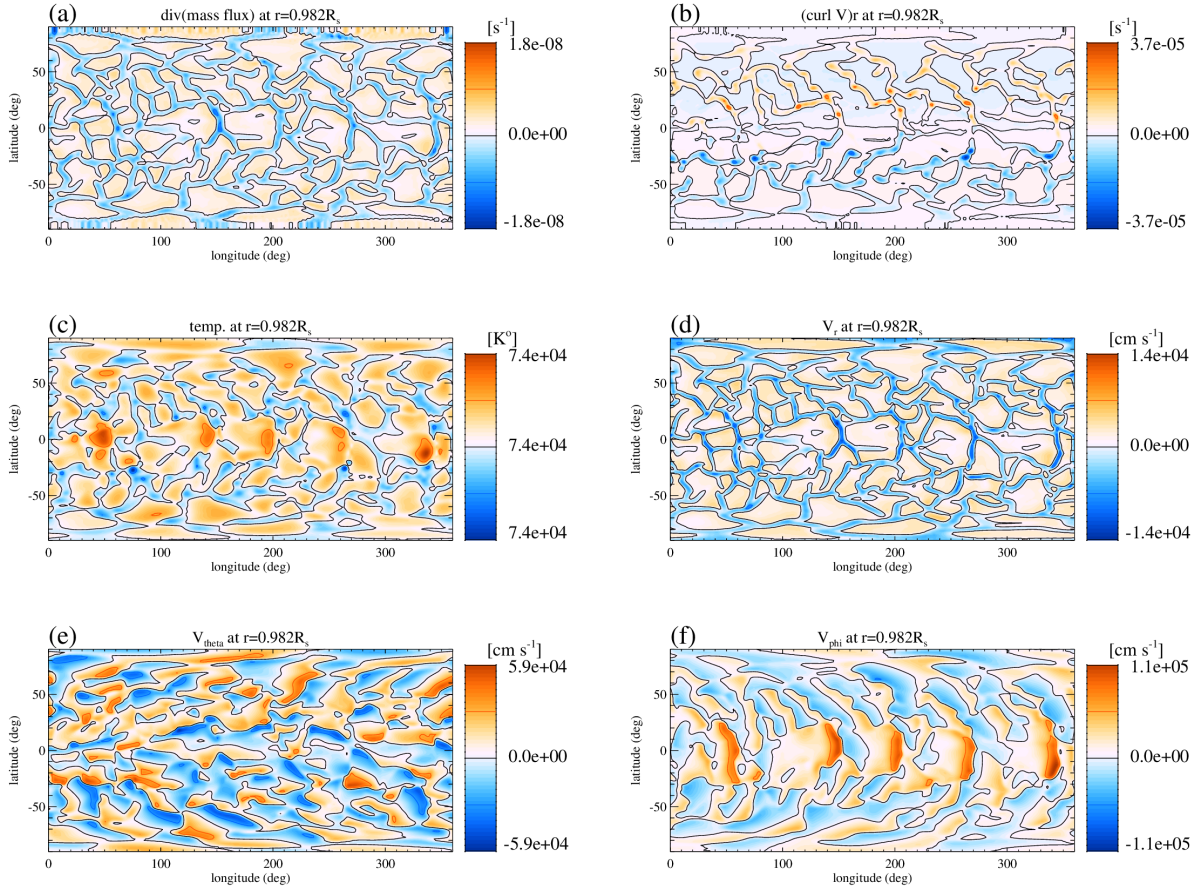


Fig. 7.— Latitude-longitude plot at $r = 0.982 R_\odot$ and $t = 10^7$ s. The colors are truncated at the largest absolute value so that the red (for positive values) and blue (for negative values) are assigned evenly across the zero values.

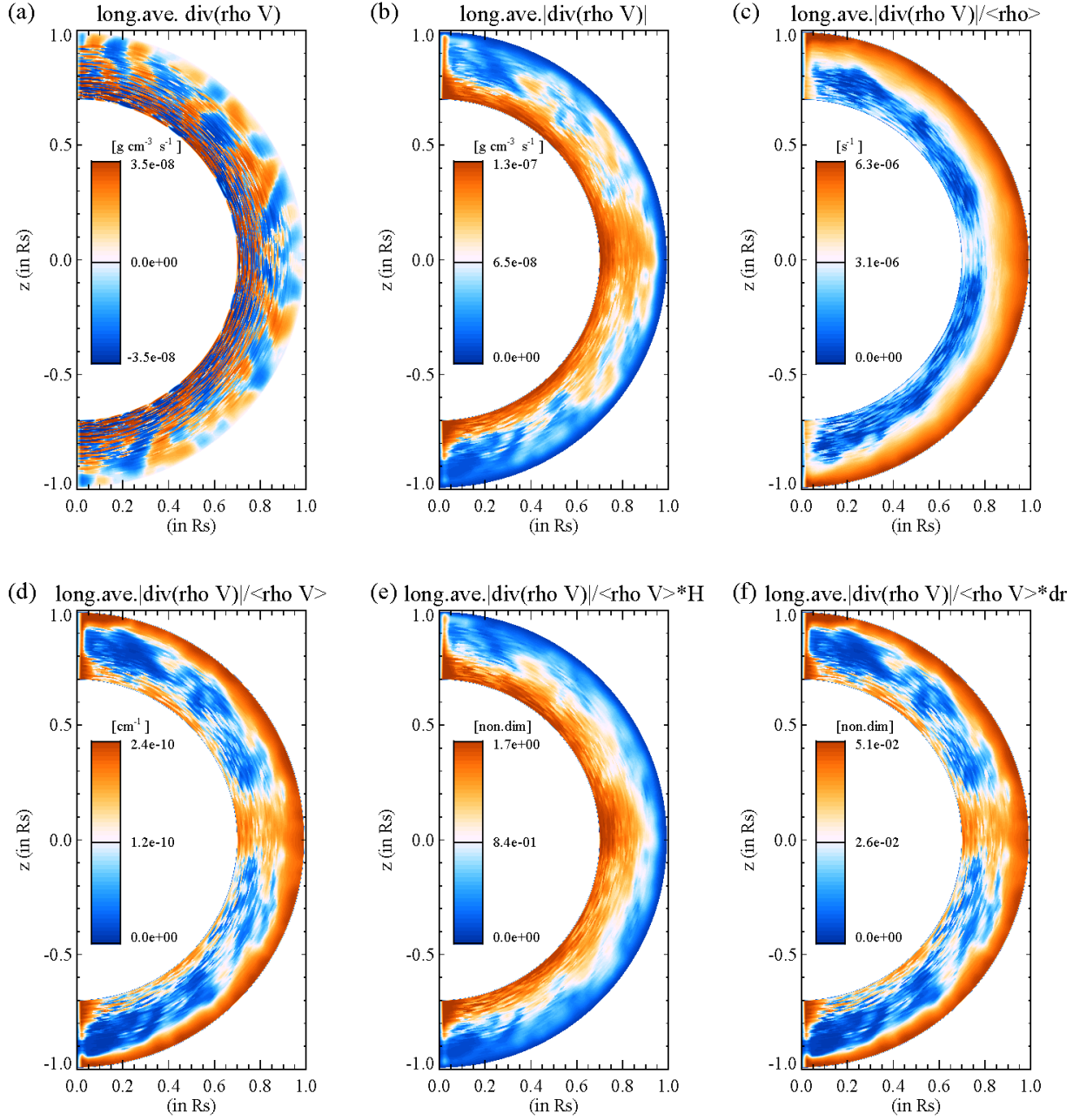


Fig. 8.— The divergence of mass flux ($\nabla \cdot (\rho \mathbf{V})$) and the normalized values in the meridional plane.

flux. The largest values are found near the top boundary, and the maxima is about $2.5 \cdot 10^{-10} \text{ cm}^{-1}$, corresponding to the spatial scale of about $4 \cdot 10^9 \text{ cm}$, comparable to the thickness of the simulated convection zone. Near the bottom boundary surface, the spatial scale is estimated to be larger. The estimated spatial scales suggest that the discrepancy between the incompressible model and compressible one is overall not significant for the global scale of the solar convection simulations with the actual solar parameters.

Figure 8(e) shows the quantity shown in panel (d) multiplied by the local scale height, $H = (d \ln \rho / dr)^{-1}$, to assess the degree of discrepancy in small volumes. The regions with values larger than 1.0 are found in the inner part of the simulated convection zone. This implies that compressibility can be one of the primary factors in determining the high-density slow-flow regions in the long term. Near the top boundary surface, the values are much smaller, indicating that the divergence of mass flux is not sufficiently large to substantially alter the background radial profile of the plasma density.

Lastly, Figure 8(f) shows similar quantities to those shown in panel (e), except that the size of the numerical cells in the radial direction is used to multiply the values in panel (d). This dimensionless value is always less than 0.063, meaning that the cell size is sufficiently small to handle the divergence of the mass flux and, hence, the temporal variation of the mass density properly.

3.5. Spatial scale in the latitudinal and longitudinal directions

Panels (a) – (d) of Figure 9 show the spherical harmonic spectral powers of the three components of the plasma velocity (V_r , V_θ , and V_ϕ) and the kinetic energy density ($\rho V^2/2$). Overall, the peaks are found around the harmonic degree (l) from 5 to 15 at any depths, and the peak values of these four parameters are larger (smaller) at the outer (inner) parts. The simulation grid size in the horizontal (perpendicular to the radial direction) is about 1 degree in the heliocentric angle, and a typical horizontal structure is captured by approximately 30 subgrid cells. The powers for the longitudinal component V_ϕ and the kinetic energy ($\rho V^2/2$) have peaks around $l \sim 5$, while the other two (V_r and V_θ) have peaks around $l \sim 10$. The powers of the plasma flow velocity become smaller as the sampling depth becomes deeper, while this tendency is not clear in the kinetic energy density.

In panels (e) and (f), the ratio of the powers of V_θ to V_r and V_θ to V_ϕ are shown. If the three components are evenly driven, then the ratio would be close to 1. As seen in these two panels, the power ratios are seldom equal or close to 1 (10^0); hence, the anisotropy in the convection zone (e.g., Guerrero et al. 2022) is significant. In the presented simulation, the radial component of plasma flow is set to zero ($V_r = 0$) on the bottom and top boundary surfaces; hence, the ratios for depths close to the boundaries tend to be larger than the others.

At the depths away from the boundary surfaces, overall, the ratio is greater than 1 for $l <$

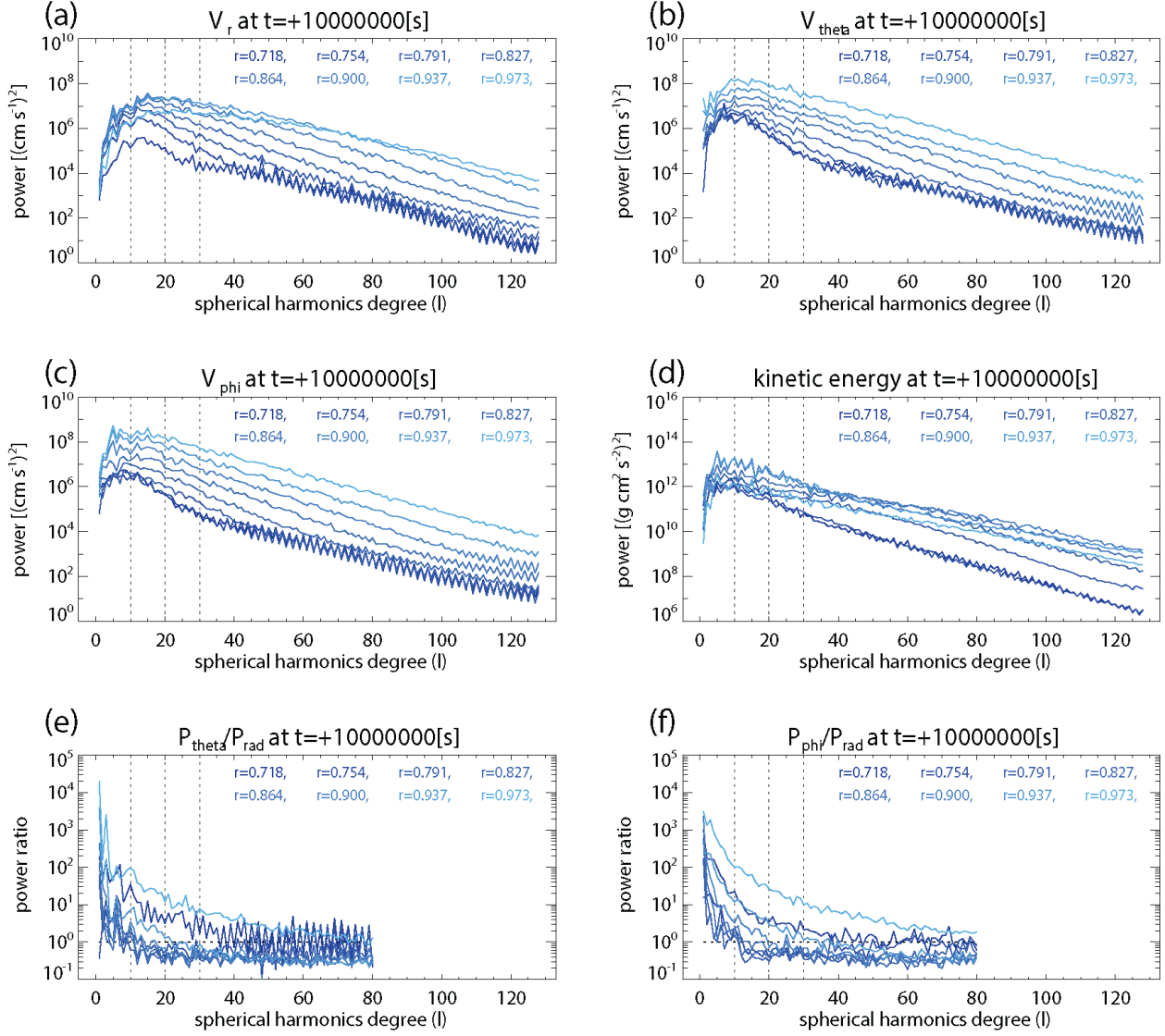


Fig. 9.— (a) – (d) Spherical harmonics spectral of three components of the plasma flow velocity (V_r , V_{θ} , and V_{ϕ}) and the kinetic energy density ($\rho V^2/2$) at various depths. (e) The ratio of the power of V_{θ} (shown in panel (b)) to that of V_r (shown in panel (a)). (f) The ratio of the power of V_{ϕ} (shown in panel (c)) to that of V_r . In panels (e) and (f), the plot lines are truncated at $l = 80$. The sampling depths are indicated with color thickness; the darker (lighter) blue for deeper (shallower) layers.

$10 \sim 20$, implying that the horizontal flows dominate over the radial flows in the large scale over the wide range of depths. For larger harmonic degrees (i.e., $l > 20$), the power ratios are rather constant at $10^{-0.3} \sim 10^{-0.4}$ or $0.4 \sim 0.5$ over the different depths; hence the square of the radial component V_r^2 and that of horizontal components $V_h^2 = V_\theta^2 + V_\phi^2$ are nearly balanced, indicating that the anisotropy of the plasma flows are small in the small spatial scale over a wide range of radius.

3.6. Long-term variations

Figures 10 and 11 show the long-term trends of plasma flows in the convection zone. In Figure 10, the three components (V_r , V_θ , and V_ϕ) at three selected depths (0.982 , 0.846 , and $0.709 R_\odot$) are shown in the time-latitude diagram to capture the latitudinal motions of the plasma flow patterns.

An interesting point is found in the top row, where the patterns of the three components appear moving poleward at $r = 0.982 R_\odot$, even when the average direction of V_θ favors the equatorward motions (as seen in panel (e) of Figure 6). This tendency becomes less noticeable in the middle of the convection zone, and the equatorward motion of the patterns is found in the deeper part of the simulated convection zone (in the bottom row).

In Figure 11, the three components (V_r , V_θ , and V_ϕ) are plotted on the longitude-time diagram. The time here runs from top to bottom, following the convention of the stack plot format. In the top row, the simulated plasma flows at the equator (noted as "lat=0" in the plot title). The prograde motions of the patterns can be clearly seen as the streaks running from top left to bottom right. This is straightforwardly related to the solar-like differential rotation shown in the meridional section view in Figure 6(f). In the middle row, the same properties but sampled at 45 degrees South are shown. The prograde motions are still noticeable. In the bottom row, the same quantities near the bottom boundary surface ($r = 0.709 R_\odot$) are shown. At this depth, no distinct tendency of the solar rotation can be found in part because of the boundary condition for the bottom boundary sphere.

4. Discussion and Summary

We conducted a hydrodynamic simulation of the solar convection zone with the CHORUS++ code. We used solar luminosity and solar rotation rate, and the results are substantially different from the benchmark tests by (Chen et al. 2023). Therefore, simulations with actual solar parameters are critically important to tackle many unanswered questions about the solar interior, solar dynamo, and solar-cycle variations (Fan 2021, and references therein).

This article offers the model descriptions and preliminary analysis of the simulation results. One item worth repeating here is the evaluation of the appropriateness of the anelastic and/or

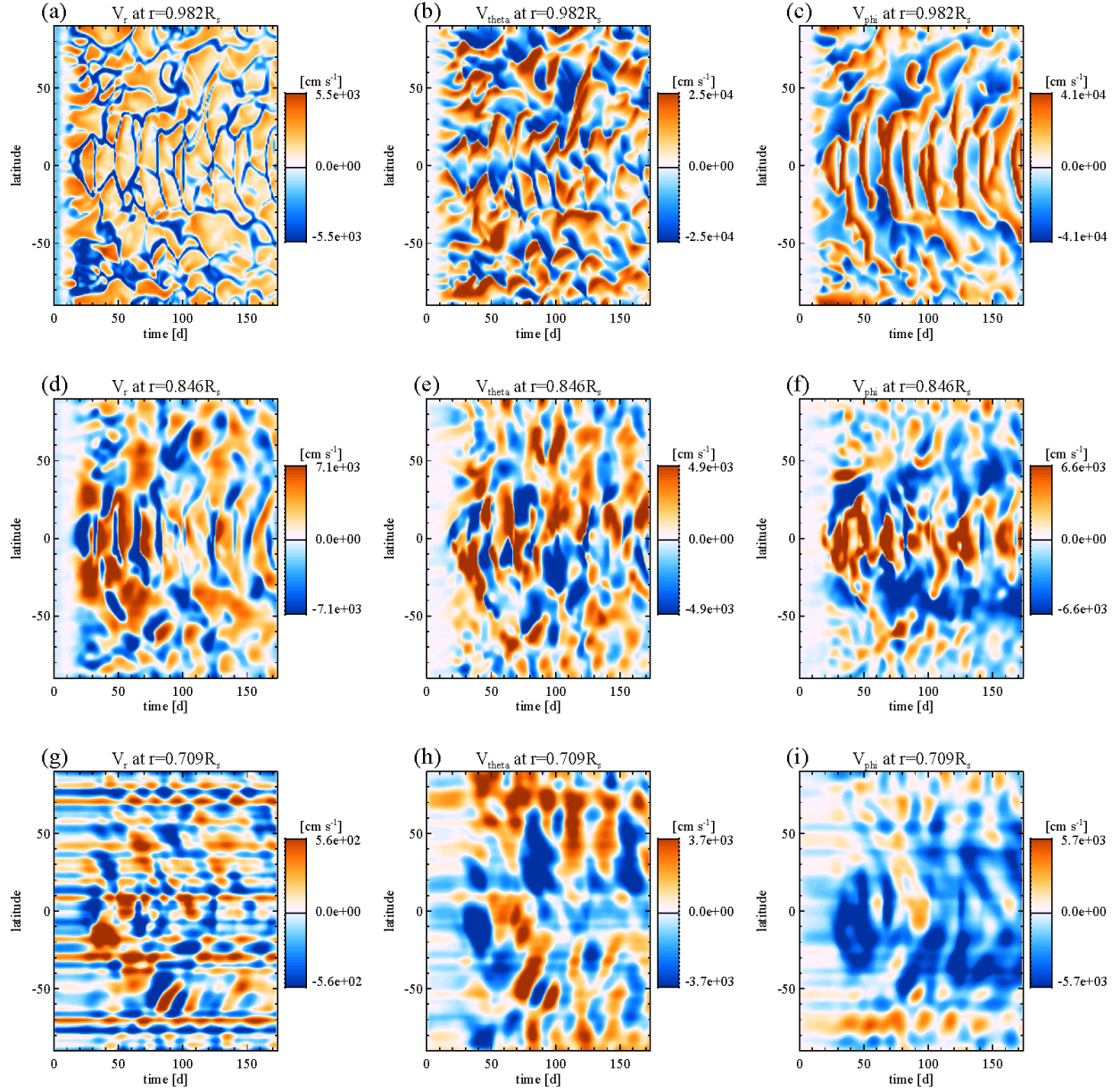


Fig. 10.— Butterfly (latitude-time) diagram of the plasma quantities. The colors were truncated at the 95 percentile of the absolute values of each variable.

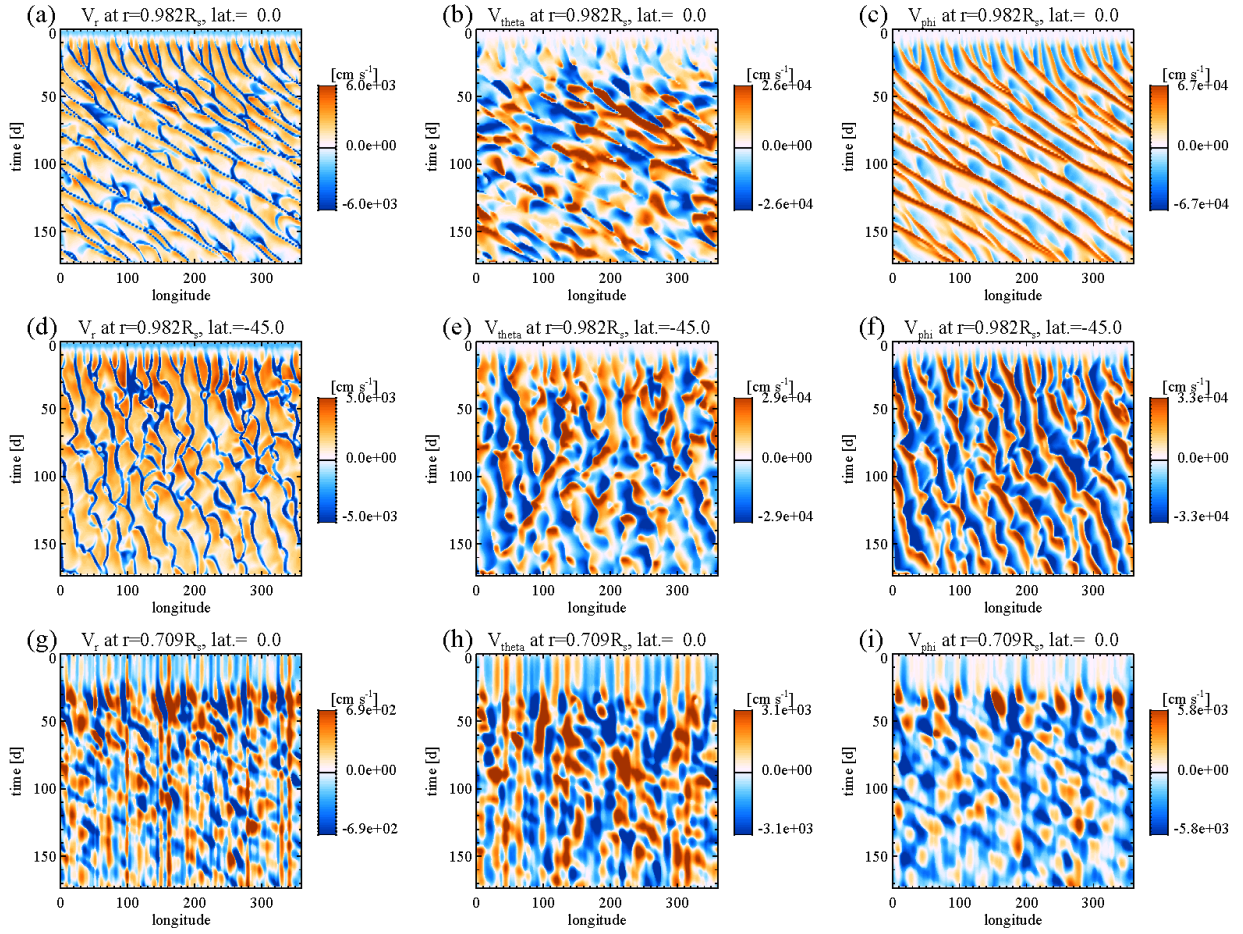


Fig. 11.— Stack plot format of the plasma flow components. The colors were truncated at the 95 percentile of the absolute values of each variable.

constant-mass assumptions that have been widely used. As shown in Section 3.4, the estimation least favoring the anelastic model still supports the divergence-free condition of mass flux and the sound-speed reduction method; in fact, the horizontal (latitudinal and longitudinal) gradients of the simulated mass density and temperature with the compressible HD code are very small with a deviation ratio of about $10^{-5} - 10^{-4}$ relative to the average except for the region close to the solar surface. Therefore, we find that the divergence-free constant-mass density assumption is appropriate for studying the dynamics of the deep solar convection zone. At the same time, small gradients of the plasma properties are the primary drivers of the plasma motions; hence, the small-amplitude fluctuation of the plasma properties can affect the long-term dynamics. An implication of this study is that the contribution of the near-surface density fluctuations must be considered when the model includes the shallow subsurface region, as the time scale there is estimated at an order of day. A critically important expansion of the convection model is to set the upper boundary surface as close to the solar surface ($r = 1 R_{\odot}$) with much higher resolution (smaller grid size) in the radial direction to capture the plasma gradients near the solar surface and properly simulate the most turbulent part of the Sun.

With a set of parameters, the solar-like differential rotation was obtained, although the meridional circulation patterns are not consistent with observations. In the presented model setting, the magnetic field is not included and the near-surface heat-escaping mechanism is simply expressed with the radiation dissipation term that is a function of radius. The results will improve or be more realistic if we include the magnetic field and MHD interactions in the convection zone (e.g., Hotta et al. 2022). The uniform heat flux is assumed at the bottom of the convection zone in the presented simulations. This assumption can be modified to examine the influence of the horizontal (latitudinal and longitudinal) gradients of the plasma quantities on the long-term solar dynamo (e.g., Bekki et al. 2024). In the presented study, we set the radial component of the plasma flow to zero $V_r = 0$ on the boundary spheres together with the stress-free conditions for the horizontal components. In the actual Sun, the penetration of convection flows into the radiation zone is possible and can have a large influence on the entire dynamics of the solar/stellar cycles (e.g., Korre & Featherstone 2024). The interactions between the convective zone and the radiation zone across the tachocline can be assessed by setting the radius of the bottom boundary surface below $0.7 R_{\odot}$ with the CHORUS++ model.

Recently, a new MHD version of the CHORUS++ model has been intensely tested (Paoli & Liang 2025). We plan on modifying and expanding the model capabilities to realistically model the dynamics of the solar interior. This new version will allow investigations of the convection dynamics that have not yet been fully understood.

This work was supported by the NASA DRIVE Center COFFIES (Consequences Of Fields and Flows in the Interior and Exterior of the Sun) grant 80NSSC22M0162. Computational resources supporting this work were provided by the NASA High-End Computing (HEC) Program through the NASA Advanced Supercomputing (NAS) Division at Ames Research Center. C.L. thanks a

National Science Foundation (NSF) award (No. 2310372).

REFERENCES

- Bassi, F., & Rebay, S. 1997, *Journal of Computational Physics*, 131, 267
- Bekki, Y., Cameron, R. H., & Gizon, L. 2024, *Science Advances*, 10, eadk5643
- Brun, A. S., Miesch, M. S., & Toomre, J. 2004, *ApJ*, 614, 1073
- Chen, K., Liang, C., & Wan, M. 2023, *Physics of Fluids*, 35, 086120
- Dikpati, M., Raphaldini, B., McIntosh, S. W., et al. 2024, *Proceedings of the National Academy of Science*, 121, e2415157121
- Elliott, J. R., Miesch, M. S., & Toomre, J. 2000, *ApJ*, 533, 546
- Fan, Y. 2021, *Living Reviews in Solar Physics*, 18, 5
- Fan, Y., Abbett, W. P., & Fisher, G. H. 2003, *ApJ*, 582, 1206
- Feng, X., Yang, L., Xiang, C., et al. 2010, *ApJ*, 723, 300
- Guerrero, G., Smolarkiewicz, P. K., de Gouveia Dal Pino, E. M., Kosovichev, A. G., & Mansour, N. N. 2016, *ApJ*, 819, 104
- Guerrero, G., Stejko, A. M., Kosovichev, A. G., Smolarkiewicz, P. K., & Strugarek, A. 2022, *ApJ*, 940, 151
- Hathaway, D. H., Upton, L., & Colegrove, O. 2013, *Science*, 342, 1217
- Hotta, H., Kusano, K., & Shimada, R. 2022, *ApJ*, 933, 199
- Hotta, H., Rempel, M., & Yokoyama, T. 2014, *ApJ*, 786, 24
- Huynh, H. T. 2007, *AIAA*, 2007, 4079
- . 2009, *AIAA*, 2009, 403
- Jones, C. A., Boronski, P., Brun, A. S., et al. 2011, *Icarus*, 216, 120
- Kitiashvili, I. N., Kosovichev, A. G., Wray, A. A., Sadykov, V. M., & Guerrero, G. 2023, *MNRAS*, 518, 504
- Kopriva, D. A. 1994, *Journal of Computational Physics*, 115, 184
- Korre, L., & Featherstone, N. A. 2024, *ApJ*, 964, 162

- Miesch, M. S., Elliott, J. R., Toomre, J., et al. 2000, *ApJ*, 532, 593
- Nagashima, K., Zhao, J., Kosovichev, A. G., & Sekii, T. 2011, *ApJ*, 726, L17
- Paoli, A., & Liang, C. 2025, arXiv e-prints, arXiv:2502.17805
- Pipin, V. V., & Kosovichev, A. G. 2024, *ApJ*, 962, 25
- Rightmire-Upton, L., Hathaway, D. H., & Kosak, K. 2012, *ApJ*, 761, L14
- Ronchi, C., Iacono, R., & Paolucci, P. 1996, *Journal of Computational Physics*, 124, 93
- Ruuth, S. J. 2005, *Mathematics of Computation*, 75, 183
- Sun, Y., Wang, Z. J., & Liu, Y. 2007, *Communications in Computational Physics*, 2, 310
- Wang, J., Liang, C., & Miesch, M. S. 2015, *Journal of Computational Physics*, 290, 90
- Wang, J., Miesch, M. S., & Liang, C. 2016, *ApJ*, 830, 45